

On the nature of the barlens component in barred galaxies

E. Athanassoula^{1*}, E. Laurikainen^{2,3}, H. Salo³, A. Bosma¹

¹Aix Marseille Université, CNRS, LAM (Laboratoire d'Astrophysique de Marseille), UMR 7326, 13388 Marseille 13, France

²Dept. of Physics/Astronomy Division, University of Oulu, FIN-90014, Finland

³Finnish Centre of Astronomy with ESO (FINCA), University of Turku, Vislntie 20, FI-21500 Pikk, Finland

Accepted . Received -

ABSTRACT

Barred galaxies have very interesting morphological features. Here we examine the barlens, a lens-like component whose extent along the bar major axis is shorter than that of the bar and whose outline is oval or circular. We show that such a component can also be found in a number of N-body plus SPH simulations. We analyse its properties by converting simulation snapshots into images, which we then analyse in the same way as images of observed galaxies. We make extensive comparisons with galaxies from the NIRSOS (Near Infrared S0 Survey) and the S4G (Spitzer Stellar Structure Survey of Galaxies) samples and find very good agreement. These comparisons include morphology, radial projected density profiles, shapes, sizes and fluxes. We observe the barlens component in our simulations from different viewing angles. This reveals that *barlenses are the vertically thick part of the bar seen face-on, i.e. that a barlens seen edge-on is a boxy/peanut/X bulge*. This finding makes it possible to follow barlens dynamics in terms of already studied families of periodic orbits. Some barlenses, notably those with near-circular projected isodensity curves, can be mistaken for classical bulges in morphological studies and classifications. This can introduce severe errors in modelling of individual galaxies, since the dynamics of classical bulges is very different from that of peanuts, and a bias in statistical morphological studies, leading to overestimates of the true frequency and mass of classical bulges. Thus, properly accounting for the barlens component will show that the fraction of disc galaxies lacking a classical bulge can be much larger than so far believed. Finally, based on the shape of the isodensity curves, we propose a rule of thumb for measuring the barlens extent along the bar major axis of galaxies sufficiently far from edge-on for the peanut not to be visible.

Key words: galaxies: spiral – galaxies: structure – galaxies: kinematics and dynamics – galaxies: evolution.

1 INTRODUCTION

To a zeroth order approximation, disc galaxies can be considered as consisting of two simple components: an axisymmetric disc and a dark matter halo. In the majority of cases, however, it is necessary to consider also at least the classical bulge and the bar, two components whose contribution to the total mass and light can be very significant and which can play an important role in the dynamical evolution of the galaxy. A more realistic picture will necessitate yet more components, such as a stellar halo, spiral arms, rings and lenses.

Furthermore, none of these components is simple. To take the bar as an example, one often sees that its description as an ellipsoid is over-simplistic and that the bar can include ansae (Sandage 1961; Laurikainen *et al.* 2007; Martínez-Valpuesta, Knapen &

Buta 2007), can have a rectangular-like outline (Athanassoula *et al.* 1990; Gadotti 2009, 2011) and, when seen edge-on, can have what is referred to as a boxy/peanut/X bulge (hereafter the B/P/X bulge), i.e. an inner part which is vertically thicker than the outer part and has the shape of a box, a peanut, or an ‘X’ (see Athanassoula 2008 for a review and references therein).

Simulations of disc galaxies have given us a lot of information on the formation and evolution of bars, the angular momentum exchanged in barred galaxies and the secular evolution that ensues (see Athanassoula 2013, for a review, and references therein). However, in order to safely apply the results of these simulations to barred galaxies and their observations, it is necessary to first make sure that they reproduce well the observed bar properties, be they morphological, photometrical, kinematical or, whenever the simulations allow it, chemical. Morphological comparisons are particularly important, since bar morphological properties have been extensively studied (see Buta 2013a and 2013b for reviews and

* E-mail:lia@lam.fr

references therein; see also e.g. Kormendy 1979, Elmegreen & Elmegreen 1985, Erwin & Sparke 2003, Buta et al. 2006 and Laurikainen *et al.* 2007). In contrast, not many simulation studies have focused on morphology. Nevertheless, considerable progress was made by Athanassoula & Misiriotis (2002), who reproduced and discussed ansae and who also found that the bar outline in strongly barred simulations was more rectangular-like than elliptical-like, in good agreement with observations (Athanassoula *et al.* 1990; Gadotti 2009, 2011).

In this paper, we will investigate a morphological feature of bars which has only lately been outlined, namely the barlens (often referred to as bl for short). These are lens-like components found in barred galaxies and first unambiguously identified, named and discussed by Laurikainen *et al.* (2011) in a study of the NIRSOS survey, where many images of galaxies with barlenses can be seen. They are shorter than bars and their outline is oval to circular-like. In the direction perpendicular to the bar major axis they are more extended than the thin bar component and they have relatively sharp edges. Further images of galaxies with barlenses can be seen e.g. in Sandage (1961), in Fig. 2 of Buta et al. (2006) and in Fig. 8 and 12 of Gadotti (2009). Here we display in Fig. 1 the NIRSOS image of NGC 4314, a characteristic barlens example (reproduced from Laurikainen *et al.* 2011 by permission). In this and many other cases one can see that the bar can be described as a sum of two components, a fat lens-like component, and a very thin and much longer component. It is the former of these components that is the barlens. A statistical study of the NIRSOS sample provided useful information on the frequency with which barlenses can be found in disc galaxies and on their sizes (Laurikainen *et al.* 2013). These observational studies, however, were not followed by any theoretical or simulation-based study. We thus ignore whether the barlens is an independent component, or a morphological feature of the bar, and know nothing on how it forms and evolves. We will aim at answering some of these questions in this paper. Further observational support for our work is presented in an accompanying observational paper (Laurikainen *et al.* 2014).

For this, we will use a number of high resolution simulations of bar formation and evolution in disc galaxies, and compare the morphology of their bars with that of the bars in the NIRSOS and the S⁴G samples. The NIRSOS sample (Laurikainen *et al.* 2011) consists of about 200 nearby early-type galaxies, mainly S0s, observed in the K_S band using 3-4 m class telescopes in good seeing conditions (full width at half-maximum 1 arcsec). The sample selection criteria include the type ($-3 \leq T \leq 1$), total magnitude ($B_T \leq 12.5$) and inclination ($i \leq 65^\circ$). The S⁴G survey (Spitzer Survey of Stellar Structure in Galaxies, Sheth et al. 2010) is an Exploration Science Legacy Program carried out on the Spitzer post-cryogenic mission. It includes more than 2300 galaxies from the nearby universe ($D < 40$ Mpc) observed with the Infrared Array Camera (IRAC) at 3.6 and 4.5 μ . Its spatial resolution is approximately 2 arcsec.

This paper is organised as follows. In Sect. 2 we summarise theoretical results relevant to bar structure and morphology and in Sect. 3 we present our simulations. In Sect. 4 we compare the morphology and the radial surface density profiles of real to that of simulated galaxies and in Sects. 5 and 6 compare the results of the ellipse fits and decompositions. We discuss all our results in Sect. 7 and conclude in Sect. 8.

2 THE STRUCTURE OF BARS

When bars form they are vertically thin, no thicker than the disc they form in. This configuration, however, is vertically not stable (Binney 1978) and, after a relatively short time, the inner part of the bar thickens considerably and protrudes clearly out of the galactic disc (Combes et al. 1990). It is important to stress that it is *not* the whole bar that thickens, but only the inner parts, the outer parts remaining thin (Athanassoula 2005). The bar can thus be considered as consisting of two parts, an outer and an inner part, the former being thin both vertically and in the equatorial plane and the latter being thick in both these directions. Let us now check how theoretical work and observations compare with this picture.

This bar structure can be easily understood with the help of 3D orbital structure (Pfenniger 1984; Skokos, Patsis & Athanassoula 2002a,b). The backbone of the bar is the x_1 family of orbits, which are periodic, planar and elongated along the bar (Contopoulos & Papayannopoulos 1980; Athanassoula et al. 1983). They are stable over most of the family extent, and thus trap regular orbits around them. This family has, nevertheless, a number of vertical instabilities, from which bifurcate other families, often called x_1v_1 , x_1v_2 , x_1v_3 etc (Pfenniger 1984; Skokos, Patsis & Athanassoula 2002a,b). Their orbits have shapes which, projected on the equatorial plane, are very similar to those of the x_1 family orbits, but, contrary to those of the x_1 , they can have a considerable vertical extent. Some of these families have important stable parts, and can thus trap regular orbits around them. These constitute the B/P/X bulge and orbital structure theory shows clearly that its extent is shorter than that of the bar (Patsis, Skokos & Athanassoula 2002). This has been well confirmed by simulations (Athanassoula 2005, and later) by measuring the length of the B/P/X bulge in a side-on¹ view, and the length of the bar in a face-on one and comparing the two lengths. Their ratio, according to orbital structure theory, can take values within a wide range, depending on which perpendicular family sets the extent of the structure. The value of this ratio was considered for the case of M31 by Athanassoula & Beaton (2006) and will be further discussed here for a number of N-body simulations. Let us now briefly review the input from observations.

In our Galaxy the bar is seen edge-on and, due to our position, is seen only after an integration along lines of sight spanning an angular extent of several degrees. For these reasons it is not possible to have a clear view of the bar morphology so that the thin and the thick bar components were initially considered as two independent bars, which, moreover, were thought to have two independent position angles and were thus assumed to rotate at different pattern speeds (Hammersley et al. 2000; Benjamin et al. 2005; Cabrera-Lavers et al. 2007; López-Corrodoira et al. 2007; Cabrera-Lavers et al. 2008; Churchwell et al. 2009). More recent work, however, argued clearly that these two bars are only the thin and the thick part of a single bar (Athanassoula 2006; Romero-Gómez et al. 2011; Martínez-Valpuesta & Gerhard 2011).

Boxy/peanut bulges can of course be easily distinguished in edge-on or near-edge-on external galaxies, since they clearly protrude out of the disc plane. Photometrically it is also possible to see that there is an associated thin component, embedded in the disc. Lütticke et al. (2000) and Bureau et al. (2006) used infrared images of samples of 60 and 30 edge-on galaxies, respectively and analysed the luminosity profile from narrow slits along or parallel to, but offset from, the major axis of each galaxy. They could

¹ In the side-on view the galaxy is observed edge-on and the line of sight is taken in the equatorial plane along the minor axis of the bar

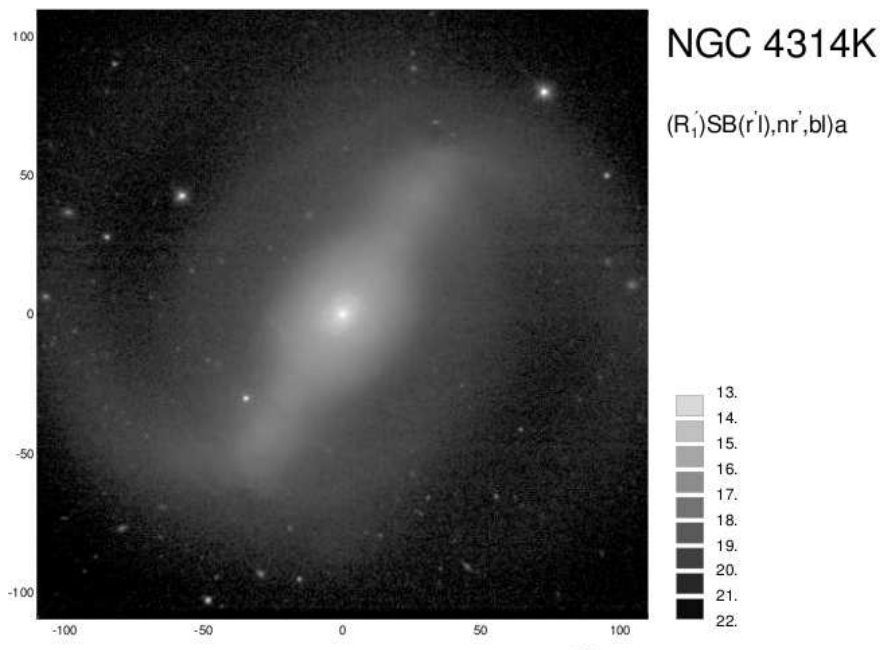


Figure 1. NIRSOS image of NGC 4314. The two components of the bar are clearly discernible. The inner component is shorter and fatter and the outer longer and more elongated (reproduced from Laurikainen *et al.* 2011 by permission).

thus verify the existence of the thin and the thick part of the bar and measure their relative extents, as well as some further relevant quantities. Unfortunately, in several cases this task can be rendered very complex by the existence of other thin components in the disc, such as lenses or rings (e.g. Wakamatsu & Hamabe 1984).

Unexpectedly, it is in inclined, but not necessarily edge-on, galaxies that the existence of the two parts of the bar can be seen easiest. This was first noted for NGC 4442 by Bettoni & Galletta (1994), for NGC 7582 by Quillen *et al.* (1997) and for M31 by Athanassoula & Beaton (2006) and Beaton *et al.* (2007), galaxies which have an inclination of 72° , 65° and 77° , respectively. N-body simulations are of course particularly well suited for such a study, because they can be viewed from any desired angle. Thus the extent of the thin part of the bar can be measured from the face-on view, while that of the thick part from the side-on one. Then the snapshot can be viewed from intermediate inclination angles in order to educate the eye to distinguish the existence and the extent of the thin and thick parts of the bar. This was first performed on a few simulations by Athanassoula & Beaton (2006), in order to obtain the necessary expertise to distinguish the bar in M31 and get information on its properties, and later by Erwin & Debattista (2013), who extended it to intermediate inclination angles and applied it to a sample of 78 galaxies. But what about the near-face-on galaxies? Answering this question is a primary goal of our paper.

3 SIMULATIONS

For our comparison with observations, we will use two groups of simulations. The first one includes simulations with gas and with spherical or triaxial haloes, each one of which will be denoted by 6 characters. The first three are ‘gtr’ (g for gas and tr for triaxial), and are common to all simulations of the group. The last three form a number which distinguishes the various simulations of the group between them. These simulations were described in some detail in

(Athanassoula *et al.* 2013, hereafter AMR13) so we will describe them here only briefly. The second group is designated by the first three letters ‘gcs’ (g for gas and cs for cusp) and has many points in common with the first group. Since no information on this group has been yet published in any paper, we will give more information here. In their initial conditions, all gtr and gcs simulations have a disc and a halo component.

All simulations were run with the GADGET code (Springel, Yoshida, & White 2001; Springel & Hernquist 2002, 2003; Springel 2005), a softening of 50 pc for all components, and a cell-opening criterion corresponding to an error tolerance for the force of 0.005. For more information on the algorithmic and numerical aspects of GADGET and the exact definition of its parameters see the manual in <http://www.mpa-garching.mpg.de/~volker/gadget> and the above mentioned references. The GADGET code offers the possibility of using several types of particles for the various components of the galaxy. In the following we will use four types, namely: HALO, DISK, GAS and STARS. The DISK particles represent stars already present in the initial conditions and their number remains constant throughout the simulation. But as the simulation evolves, new stars (STARS) form from gas (GAS), so that the number of GAS particles decreases, while that of STARS increases. At all times, the DISK particles and the STAR particles together represent the stars of the galaxy. Thus the DISK component describes older stars than the STARS component. But all the STARS do not represent young stars. Indeed, a fair fraction of them were formed during the first two Gyr and thus have similar dynamics to that of DISK particles. The main difference between the two components is that all the DISK particles represent the old stellar population, while a fraction of the STARS describe the young stellar population. This fraction, however, is a strongly decreasing function of time (see Fig. 2 of AMR13), because our simulations do not include accretion.

All simulations have initially a disc (stellar and gaseous) and

a halo component. The disc has in all cases the same initial azimuthally averaged density distribution, namely

$$\rho_d(R, z) = \frac{M_d}{4\pi h^2 z_0} \exp(-R/h) \operatorname{sech}^2\left(\frac{z}{z_0}\right), \quad (1)$$

where R is the cylindrical radius, M_d is the disc mass, h is the disc radial scale length and z_0 is the disc vertical scale thickness. They also have the same radial velocity dispersion profile, namely

$$\sigma_R(R) = 100 \cdot \exp(-R/3h) \text{ km s}^{-1}. \quad (2)$$

For all gtr runs the DISK component has a radial scale length of $h = 3$ kpc, a scale height of $z_0 = 0.6$ kpc, and the mass of each individual particle is $m_{\text{DISK}} = 2.5 \times 10^5 M_\odot$. The corresponding numbers for the gcs simulations are $h = 4$ kpc, $z_0 = 0.6$ kpc, and $m_{\text{DISK}} = 6.25 \times 10^4 M_\odot$.

For the gas we adopt the same radial profile and the same scale length as for the stellar disc. This is necessary in order to be able to make sequences of models where only the gas fraction changes but the rotation curves stay the same for all practical purposes. The gas scale height is considerably smaller than that of the stars and its precise value is set by the hydrostatic equilibrium achieved during the iterative calculation of the initial conditions (Rodionov & Athanassoula 2011).

The main difference between the two groups is the halo, gtr simulations having a core in the inner regions and gcs ones a cusp². For gtr simulations the haloes have been built so as to have, within the allowed accuracy, in all cases the same spherically averaged initial radial profile, namely

$$\rho_h(r) = \frac{M_h}{2\pi^{3/2}} \frac{\alpha}{r_c} \frac{\exp(-r^2/r_c^2)}{r^2 + \gamma^2}, \quad (3)$$

where r is the radius, M_h is the mass of the halo and γ and r_c are the halo core and cut-off radii, respectively. The parameter α is a normalisation constant defined by

$$\alpha = [1 - \sqrt{\pi} \exp(q^2) (1 - \operatorname{erf}(q))]^{-1}, \quad (4)$$

where $q = \gamma/r_c$ (Hernquist 1993). In all simulations we take $\gamma = 1.5$ kpc, $r_c = 30$ kpc and $M_h = 2.5 \times 10^{11} M_\odot$. The mass of each halo particle is equal to $m_{\text{halo}} = 2.5 \times 10^5 M_\odot$. In this group, we consider three different initial halo shapes: spherically symmetric (halo 1), mildly triaxial with initial equatorial and vertical axial ratios 0.8 and 0.6 (halo 2), respectively, and strongly triaxial with initial axial ratios 0.6 and 0.4 (halo 3), respectively. As shown in AMR13, these haloes evolve with time and their shapes become near spherical for halo2 and mildly triaxial for halo 3.

For all gcs simulations, the dark halo is modelled as a truncated NFW halo (Navarro, Frenck & White 1996, 1997)

$$\rho_h(r) = \frac{C_h \cdot T(r/r_t)}{(r/r_h)(1 + r/r_h)^2}, \quad (5)$$

where $T(x) = \exp(-x^2/r_t^2)$, r_h is the halo scale length, C_h is a parameter defining the mass of the halo, and r_t is a characteristic radius for the tapering. For all gcs models discussed here $r_h = 11$ kpc and $r_t = 50$ kpc. For halo 4 models $C_h = 0.0015$ and for halo 5 ones $C_h = 0.002$. In each of these simulations there are 2 million particles in the halo.

The initial conditions of both groups were built using the iterative procedure (Rodionov et al. 2009; Rodionov & Athanassoula

2011). To measure of bar strength during the evolution, we use in all cases the maximum of the relative $m=2$ Fourier component, as described in AMR13. The rotation curves of gtr models are given in Fig. 1 of AMR13. The list of the runs analysed here, together with their initial gas fraction and halo type are listed in Tables 1 and 3.

The next step is to use snapshots of the stellar disc component in order to create mock images in form of fits files, which will be analysed in the same way as the observed fits images of galaxies. Due to the relatively small differences between the density distributions of the DISK and STARS, we used these two components together in order to improve the signal-to-noise ratio by increasing the number of particles. In any case in real galaxies both young and old stars are observed. The analysis consists mainly of ellipse fits and decompositions, and the techniques and results are described in Sect. 5 and 6.

4 GLOBAL COMPARISONS: MORPHOLOGY AND RADIAL SURFACE DENSITY PROFILES

A simple perusal of the face-on views of the gtr snapshots shown in Figs. 4 and 5 in AMR13 shows clearly that, like in observations, simulated bars are not simple ellipsoidal objects, but have a more complex geometry. In fact the central part of the bar is considerably thicker in the equatorial plane than the outer thin bar part and has a lens-like form. A more detailed visual inspection shows that, morphologically at least, these central components, had they been observed in galaxies, would have been classified as barlens components. In the remaining of this paper we will deepen and substantiate the comparison between barlenses in real galaxies and their counterparts in simulations, and, after establishing that the latter should be called barlenses, we will examine in detail their properties in order to get more information on the barlens structures.

Let us start with comparisons including the morphology and the radial density profiles (Figs. 2, 3 and 4). Fig. 2 compares the results from five simulated galaxies (two left columns) to those of five galaxies from the NIRS0S survey, or from the S⁴G survey (two right columns). We extended this exercise to many more snapshots and galaxies, but we will limit ourselves here to five for brevity. It is important to note that the five simulations shown here were not run specifically so as to model the five chosen galaxies, they were simply picked out by a cursory visual inspection of the images of several snapshots of our gtr and gcs simulations as reasonable matches to the five chosen galaxies. Nevertheless, we get a good resemblance, both for the images and the radial projected density profiles in the region we examine, i.e. a rectangular region of linear extent somewhat larger than the bar region and including, whenever relevant, the inner ring.

The upper row compares simulation gtr106, viewed at a time $t=6$ Gyr after the beginning of the simulation, with a S⁴G image of the galaxy IC 5240. This comparison involves two of the longest and most elongated barlenses and quite strong bars. As can be seen in the second panel from the left, the bar projected surface density profiles are quite flat, arguing for a strong bar (see Elmegreen & Elmegreen 1985 for the observations and Athanassoula & Misiriotis 2002 for the simulations). Indeed, it was found in AMR13 that gtr106 was one of the strongest bars in that set of simulations (see in particular Figs. 4, 5, 7 and 8 in that paper and the corresponding discussions). In this example the extent of the bar outside the barlens is very small, the smallest amongst the examples shown in Fig. 2. Note also that in both cases, there is an X-shape in the central

² In radial profiles with a core, the density levels off as one reaches the centre. while in cuspy profiles it keeps increasing with decreasing radius.

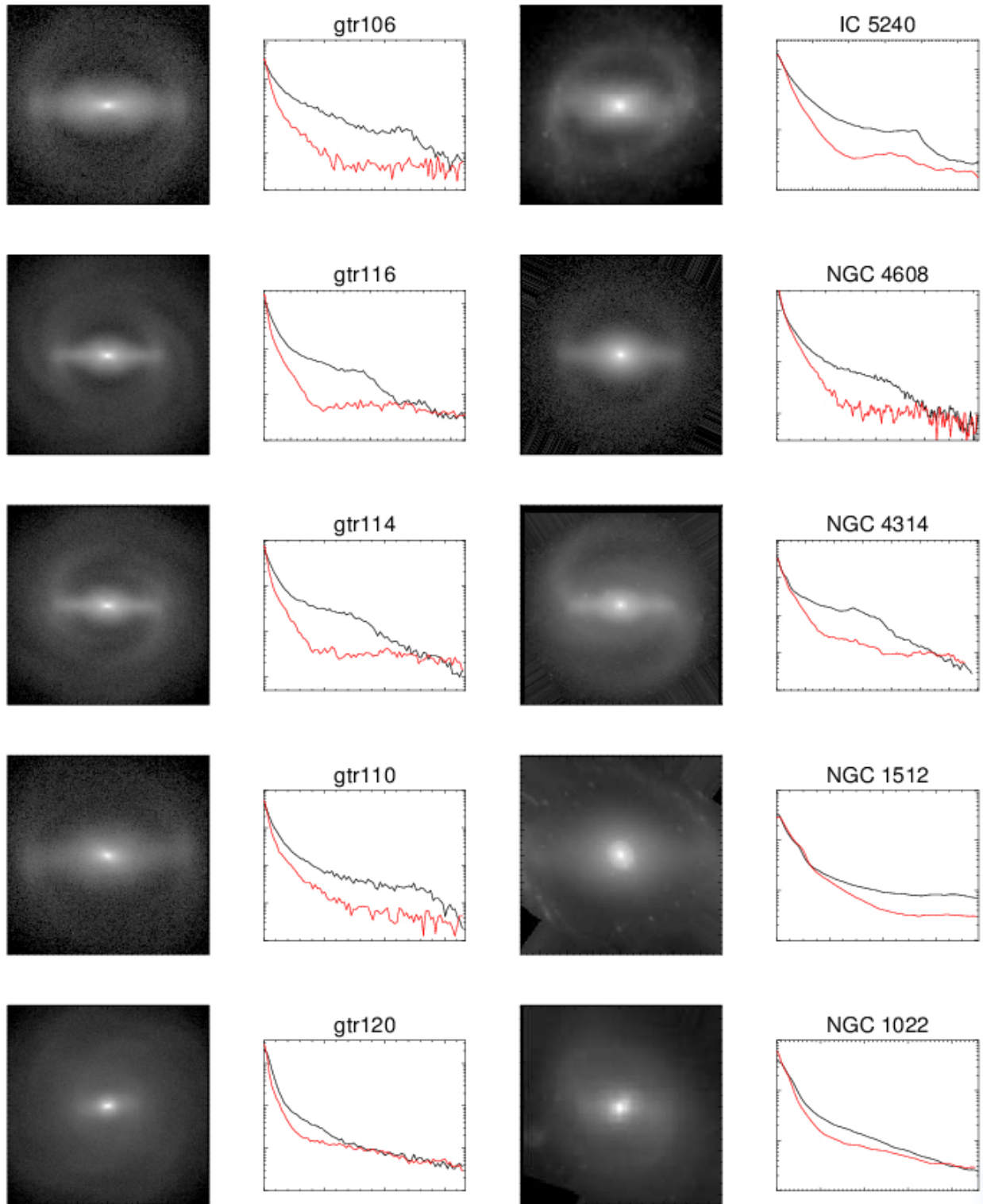


Figure 2. Images and the corresponding surface brightness profiles shown along the bar major (black lines) and minor axis (red lines in the online version). The left panels show the simulation models and the right panels galaxies with similar barlenses. The extent of the images has been chosen so as to display the same region of the galaxy, namely the bar region and, whenever relevant, the inner ring. The galaxy images are either K_s -band images from the NIRSOS Atlas, or $3.6 \mu\text{m}$ images from the S⁴G survey. Both the simulations and the galaxies are shown in face-on view, and rotated so that the bar appears in a horizontal position. The profiles show the same regions as the corresponding images. The name of the galaxy, or of the simulation is given above the corresponding radial surface brightness panel.

regions, even though the simulated galaxy is seen exactly face-on and IC 5240 quite far from edge-on. Such a behaviour is discussed in detail in the accompanying observational paper (Laurikainen *et al.* 2014).

The second row from the top compares the $t=6$ Gyr image of gtr116 with the NIRS0S image of NGC 4608. In this case, the relevant extent of the thin part of the bar – relative to both the extent of the barlens and the size of the inner ring – is much longer than in the previous example. Note also how thin in the equatorial plane the part of the bar outside the barlens is in the face-on views of both the galaxy and the simulation snapshot. Further discussion on NGC 4608 is given in Sect. 6.3.1.

The third row compares the $t=6$ Gyr image of gtr114 with the S^4G image of NGC 4314. Both have a fairly round barlens and a strong thin bar component. In the fourth row we compare gtr110 at $t=6$ Gyr with the S^4G image of NGC 1512. Here the barlens is similar to that in the two previous models, but the thin bar is considerably less pronounced, and more dispersed.

Finally, in the bottom row we compare the $t=6$ Gyr image of gtr120 to the S^4G image of NGC 1022. This is the weakest bar in this comparison, and one of the weakest bars in the AMR13 simulations. This can be witnessed also from the radial surface density profiles, which shows clearly that the difference between the profiles along the directions of the bar major and minor axes is less than in the previous cases and that the bar has an exponential profile, which according to Athanassoula & Misiriotis (2002) is a sign of a weaker bar than those those having a flat profile. In contrast, the barlens is still very prominent.

Fig. 3 compares the radial projected surface density profiles along the direction of the major axis of the bar of gtr115 and NGC 5101. Their barlens regions look remarkably similar, although the former was not made specifically so as to model the latter. There is also a further point to note in this figure, which can also be seen in the radial profiles of Fig. 2. The end of the thin bar component can be easily distinguished on these profiles because of a clear jump, or step of the radial profile at this radius. On the contrary, the profile has no feature indicating the end of the barlens and in fact, if it were only from such profiles one could not have had any estimate of the barlens semi-major axis and even not of the existence of the barlens component. This is presumably because the thin part of the bar extends inwards into the barlens region and thus the profile along the bar major axis includes contributions from both components. It will be discussed further in Sect. 7.2.

5 ELLIPSE FITTING: TECHNIQUE AND RESULTS

5.1 Technique

The fitting procedure used here is, on purpose, as similar as possible to that used for the NIRS0S galaxies. Given the complex morphological structure of bars, any automatic ellipse fitting would not give useful information concerning the barlens component. For example, isophotes corresponding to the outer regions of the barlens will also trace regions of the outer part of the thin bar component and any automatic ellipse fit would be a compromise between the shape of the barlens and that of the thin outer parts of the bar. Thus, such fits would be biased and useless for our purposes. We therefore resorted to a fully interactive fitting procedure, which, although much more time consuming, guarantees relevant fits.

For the simulation galaxies, before starting the measurements, the simulation units of the image were converted to magnitudes

Table 1. Ellipse fitting results for the barlenses (bl) and the thin part of the bar (bar) in simulation results at time $t=6$ Gyr.

run	Halo profile	gas [%]	b/a (bl)	r_{bl}/r_{bar}
gtr101	1: core/spherical	0	0.43	0.77
gtr106	1: core/spherical	20	0.65	0.57
gtr111	1: core/spherical	50	0.95	0.37
gtr116	1: core/spherical	75	0.93	0.45
gtr119	1: core/spherical	100	0.74	0.56
gtr102	2: core/mildly triaxial	0	0.45	-
gtr209	2: core/mildly triaxial	20	0.74	0.47
gtr114	2: core/mildly triaxial	50	0.88	0.46
gtr117	2: core/mildly triaxial	75	0.89	0.81
gtr120	2: core/mildly triaxial	100	0.94	0.51
gtr110	3: core/strongly triaxial	20	0.68	0.49
gtr115	3: core/strongly triaxial	50	0.93	0.52
gtr118	3: core/strongly triaxial	75	0.88	0.53
gtr121	3: core/strongly triaxial	100	0.88	-
gcs006	4: NFW1	0	0.64	0.94
gcs001	4: NFW1	20	0.89	0.46
gcs002	4: NFW1	40	0.96	0.44
gcs003	4: NFW1	60	0.90	0.52
gcs004	4: NFW1	80	0.95	-
gcs009	5: NFW2	60	0.74	0.56
gcs010	5: NFW2	80	0.91	0.46

by logarithmic transformation, using a magnitude zero-point of 24 mag/arcsec². The subsequent procedure was followed identically for observed and for simulated galaxies. All images were inspected to determine the magnitude range in which the barlens is best visible, and this was systematically used in all further measurements. Each individual galaxy was then visualised and points on the outermost edge of the barlens were chosen by eye. An ellipse was fitted to these points and its parameters stored for further analysis.

The important advantage of our approach is that measurements are not affected by the narrow outer part of the bar (thin bar component), which in automatic ellipse fitting would erroneously make the barlens too elongated.

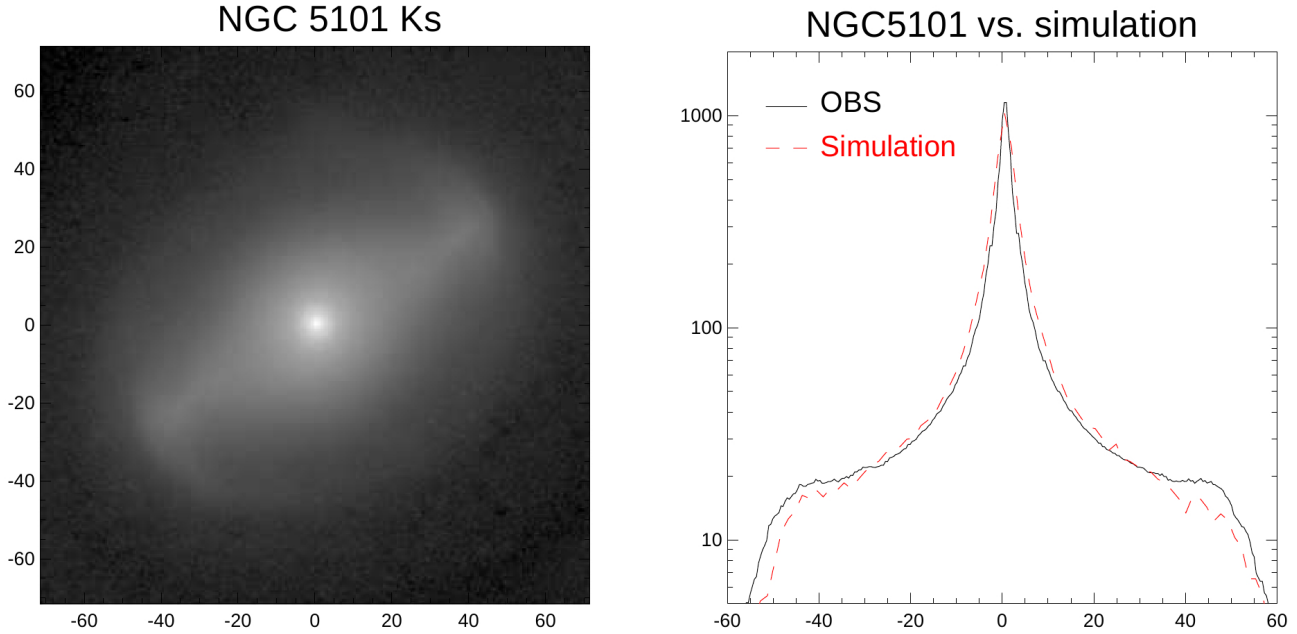


Figure 3. Left panel: The bar region of NGC 5101 in the Ks band (from the NIRS0S sample). Right panel: The surface brightness profiles of the simulation model gtr115 at $t = 6$ Gyr (dashed line, red in the online version) and NGC 5101 (full black line), both shown along the bar major axis. As in the previous figure, only the bar region is shown, so that the sharp edge in the profile is a manifestation of the edge of the bar.

Table 2. Evolution of the ellipse fitting results with time for the barlens (bl) and the thin bar component (bar) in four simulations.

Time [Gyr] ->	5	6	7	8	9	10
<i>gtr101:</i>						
$b/a(bl)$	0.59	0.53	0.50	0.47	0.44	0.43
r_{bl}/r_{bar}	0.61	0.78	0.86	0.84	0.98	1.00
<i>gtr111:</i>						
$b/a(bl)$	0.93	0.95	0.53	0.64	0.79	0.83
r_{bl}/r_{bar}	0.39	0.34	0.74	0.69	0.56	0.57
<i>gtr119:</i>						
$b/a(bl)$	0.72	0.69	0.79	0.79	0.72	0.75
r_{bl}/r_{bar}	-	0.61	0.53	0.61	0.64	0.61
<i>gcs004:</i>						
$b/a(bl)$	0.86	0.95	0.91	0.93	0.89	0.96
r_{bl}/r_{bar}	-	-	-	-	-	0.36

Bar lengths were measured in a similar manner by visually marking the outer edges of the bar. In cases when the simulation model has an inner ring there is some ambiguity because the bar can be considered to end where the ring starts, or to continue all through the ring, i.e. to end at the outer extremity of the ring. Here we follow the same definition as in the NIRS0S observations, namely that the end of the bar is defined by the ridge-line of the ring. Which of the three estimates is best is debatable, but it is of no concern here since all we need for comparisons is to use the same method and bar length definition for the simulations as for the observations in order to allow comparisons, particularly since the bar length estimate will be used further in the decompositions (see Sect. 6).

5.2 Results

Table 1 gives information on the ellipses fitted to the face-on images of the simulation snapshots at time $t = 6$ Gyr from the beginning of the run. The first three columns give the simulation name, its halo characteristics and its initial gas fraction, respectively. The fourth and fifth columns give the axial ratio of the barlens component and its extent normalised by the bar length. The five packages in this Table correspond to the five different halo radial profiles, halo 1 to halo 5, described in Sect. 3. In this, as in all subsequent tables, a dash as an entry means that no safe estimate for this quantity could be found. This occurs particularly, but not exclusively, in cases like gcs004 or gtr121, where the thin part of the bar is so weak that it is very hard to measure its extent reliably. Results from different viewing angles will be discussed later (see Table 5 and Sect. 6.3.3).

Note that no cases of very elongated barlenses were found, the two most elongated ones being for gtr101 (0.43) and gtr102 (axial ratio 0.45), both cases being simulations with no gas and amongst the strongest bars in AMR13. In all the other cases the barlenses are considerably nearer to near-circular, with most axial ratios between 0.7 and 1.0. The ratio of the extents of the barlenses to the thin bar component has a lower limit of ~ 0.4 and an upper one of ~ 0.9 . We will discuss the implications of this result in Sect. 7.5.

Table 2 also gives information on the barlens shape and on the ratio of its extent with that of the bar, now as a function of time and for only a few simulations. It shows that the fractional change of the barlens shape, as well as of its extent relative to the bar vary considerably from one case to another. The least variation is found for gcs004, where the changes are barely of the order of 10 per cent, and the most for gtr101 where the changes are nearly of the order of 50 per cent. In general we can see that the runs that showed the most secular evolution (see AMR13) show also the largest changes of the measured quantities, as expected. We will discuss this further

in Sect. 7.4. Simulation gtr111 has a rather complex behaviour with two distinct time intervals in the evolution of different properties for the barlens. For times up to and including 6 Gyr the barlens is near-circular, with axial ratios larger than 0.9, then shows a rather abrupt jump between 6 and 7 Gyr, while from 7 Gyr onward it is considerably more elongated, with an axial ratio value (extent ratio value) 0.53 and 0.83 (0.56 and 0.54). It is interesting to note that the increase of the bar strength with time shows a change of slope between $t = 6$ and 7 Gyr (AMR13), i.e. at roughly the same time when the change in the axial ratio of the barlens occurs. This constitutes a further argument for a strong link between the barlens and the bar.

6 DECOMPOSITIONS: TECHNIQUE AND RESULTS

6.1 The components

The simulation models discussed in the previous section were decomposed into multiple structural components, fitting also the bar with two separate functions. We used GALFIT (Peng et al. 2010; with the auxiliary illustration programs described in Salo *et al.* 2014) and the same approach as that used for the observed images in the NIRS0S Atlas (Laurikainen *et al.* 2010). For the weighting of the simulation images a constant sigma-image was used because this mimics well the typical uncertainty map for ground based near-IR images, where the noise is dominated by the sky background. All fitting functions have generalised elliptical isophotes (Athanassoula *et al.* 1990), so that:

$$r = (|x|^c + |y/q|^c)^{1/c} = 1,$$

where c is a shape parameter, $q = b/a$ and a and b are the major and minor axes, respectively. An isophote is boxy when its shape parameter $c > 2$, diamond-like when $c < 2$, and elliptical when $c = 2$. For the radial projected surface density of the disc component we used an exponential function:

$$\Sigma(r) = \Sigma_{0,d} \exp[-(r/h_r)],$$

where $\Sigma_{0,d}$ is the disc central surface density, and h_r is the disc radial scale length. The thin bar component is described by a modified Ferrers function:

$$\Sigma(r) = \Sigma_{0,th} (1 - (r/r_{out})^{2-\beta})^\alpha,$$

where $\Sigma_{0,th}$ is the central surface density of the thin bar component, r_{out} is its outer edge, β gives its central slope, and α is a measure of the sharpness of its outer truncation (Ferrers 1877). The barlens component was fitted by a Sérsic function:

$$\Sigma(r) = \Sigma_{0,bl} \exp[-(r/h_{bl})^{1/n}],$$

where $\Sigma_{0,bl}$ and h_{bl} are the barlens central surface density and its scale parameter, respectively, or alternatively with a Ferrers function, when this allowed for better fits.

There are two important points to note in the above choices of the components and of their properties. The first one is that we adopted generalised ellipses, which is particularly important for the thin bar and barlens components, because their isophotes do not have an elliptical shape. The second is that we describe the bar as a sum of two components, namely the barlens and the thin bar component, which is essential for the correct representation of the bar, as will be seen from Tables 3 and 4.

Table 3. Flux ratios of the barlens component as obtained from the decompositions of snapshot images at $t = 6$ Gyr.

run	Halo	gas [%]	F_{bl}/F_{thin}	F_{bl}/F_{tot}
gtr106	1: core/spherical	20	2.6	0.33
gtr111	1: core/spherical	50	0.93	0.13
gtr116	1: core/spherical	75	1.2	0.15
gtr119	1: core/spherical	100	2.5	0.13
gtr209	2: core/mildly triaxial	20	3.1:	0.39
gtr114	2: core/mildly triaxial	50	3.5	0.25
gtr117	2: core/mildly triaxial	75	0.4	0.26
gtr120	2: core/mildly triaxial	100	9.5	0.19
gtr110	3: core/strongly triaxial	20	6.7	0.44
gtr115	3: core/strongly triaxial	50	1.9	0.19
gtr118	3: core/strongly triaxial	75	3.9	0.14
gtr121	3: core/strongly triaxial	100	-	0.18
gcs001	4: NFW1	20	-	0.21
gcs002	4: NFW1	40	2.9	0.18
gcs003	4: NFW1	60	3.5	0.20
gcs009	5: NFW2	60	2.3	0.18
gcs010	5: NFW2	80	4.4	0.21

6.2 The fitting procedure

In our GALFIT decompositions we used the same procedure as in observational studies (Laurikainen *et al.* 2010). The bar length was set to be the visually estimated outer edge of the bar obtained during the ellipse fitting work (Sect. 5). This was reasonable, because otherwise GALFIT would try to consider the inner ring as part of the bar. After that, the fitting process was iterative, and a large number of trials were made until a ‘final’ decomposition was adopted. The choice was based on inspecting the profile fitting, and on a comparison of the decomposition model with the image. Generally, it was not possible to get good fits by setting free all parameters at once. We thus fixed some values and let GALFIT search for the remaining. Once a reasonable value was found for one parameter, it was fixed and others set free. These cycles were continued until the final decomposition was reached. The number of necessary trials varied from one image to another, but was always large. Also the sequence in which we freed parameters varied from one case to another, although we often found easiest to find first reasonable values for the orientations, the fluxes and the disc scale length.

6.3 Results

6.3.1 Comparing decomposition results for an observed and a simulated galaxy

Fig. 4 compares the decomposition results for NGC 4608 from the NIRS0S sample and simulation gtr115. The left panels show the respective images and the middle ones the superposition of the components resulting from the decompositions. Already from here we can see that the simulation snapshot describes the galaxy quite successfully, even though it was not made specifically for that purpose but is just a closely resembling snapshot from the AMR13 sample. This comparison is made more quantitative in the right panels, which show the radial surface density profiles of the various components separately, as well as the totals. Such plots are standard

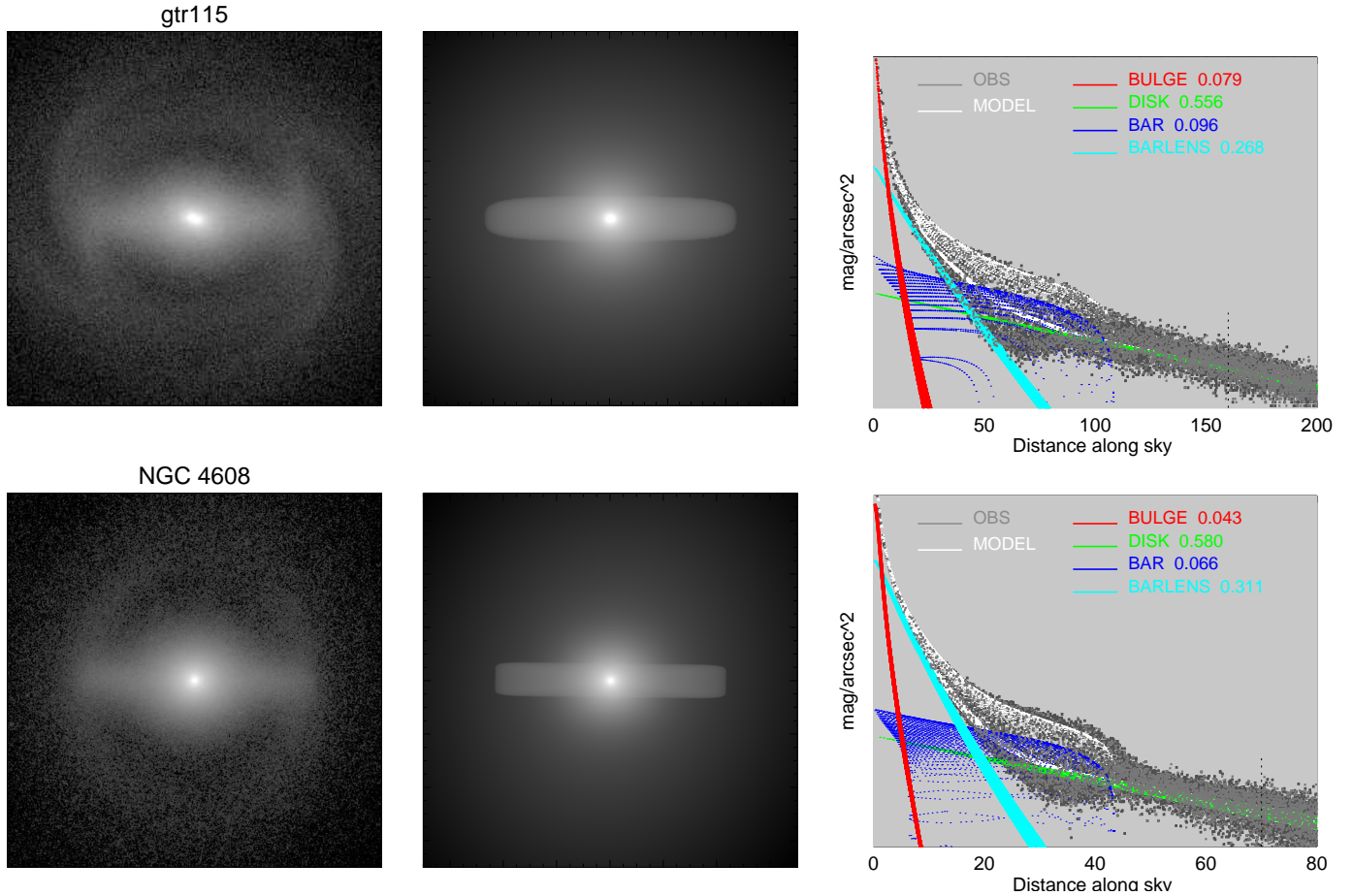


Figure 4. Images and their decompositions for the simulation model gtr115 (upper panels), and the galaxy NGC 4608 observed in K_s -band (lower panels). The left panels show the images and the middle ones show the sum of the components obtained from their decomposition. All the images are shown in face-on view and cut so as to show only the bar and inner ring region. The right panels show two dimensional representations of the surface brightness profiles of the images (black dots), as well as of the GALFIT decomposition models fitted for the different structure components (red dots for the bulge, green for the disc, dark blue for the bar and cyan for the barlens). The total decomposition models are shown with white dots. ‘Bar’ in the profile refers to the thin bar component and ‘barlens’ is the thick, fairly round component. The method and the functions used for making the decompositions are described in the text. The abscissa in the lower right is given in arcseconds. In the upper right panel the abscissa is scaled so that the bar length is roughly the same for the galaxy and for the simulation. The vertical black dotted lines in the profile figures (roughly at a distance from the centre of 160 and 70 pixels for the upper and lower panels, respectively) show the edges of the images in the left and middle panels.

in observational studies and are made so as to include information from non-axisymmetric 2D decompositions in radial profiles. Every black point is a pixel from the image and every red (green, dark blue and cyan) point is a pixel from the bulge (disc, bar and barlens component, respectively). Thus this plot can be seen as a sequence of radial surface density profiles for each component separately, the total model and the image. It shows clearly that the simulation represents very well NGC 4608.

6.3.2 Decomposition results for a number of simulations and times

In Tables 3 and 4 we give the decomposition results for the flux ratios of all models for which we measured the ellipticities. The former has the same layout as Table 1, except that in the fourth column we give the values of the barlens fluxes normalised to the flux of the thin bar component, F_{bl}/F_{thin} , and in the fifth one the same quantity, now normalised to the total flux of the galaxy, F_{bl}/F_{tot} .

Table 4. Time evolution of the relative flux of the barlens component, as obtained from decompositions of the simulation images.

Age ->	4	5	6	7	8	9	10
[Gyr]							
<i>gcs004:</i>							
F_{bl}/F_{thin}	19.20	19.20	8.44	8.44	12.11	7.82	10.86
F_{bl}/F_{tot}	0.19	0.19	0.21	0.21	0.22	0.22	0.23
<i>gtr111:</i>							
F_{bl}/F_{thin}	0.44	0.81	0.95	-	2.35	1.39	1.36
F_{bl}/F_{tot}	0.03	0.08	0.13	-	0.22	0.20	0.21
<i>gtr119:</i>							
F_{bl}/F_{thin}	6.16	6.28	5.81	2.87	2.53	1.79	1.79
F_{bl}/F_{tot}	0.11	0.16	0.16	0.16	0.17	0.20	0.20

Table 5. The effect of the viewing angle on the properties of barlenses for the simulation model gtr111 at time $t=6$ Gyr

Bar position angle	inclination	b/a	F_{bl}/F_{thin}	F_{bl}/F_{tot}
00	00	0.96	0.95	0.130
00	30	0.77	0.95	0.110
00	60	0.64	0.50	0.054
30	30	0.80	0.99	0.116
30	60	0.78	0.79	0.089
60	30	0.75	1.30	0.135
60	60	0.66	0.31	0.058
90	30	0.83	0.66	0.107
90	60	0.86	1.07	0.118

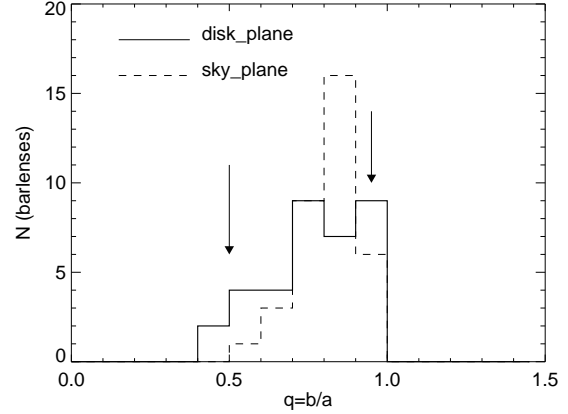
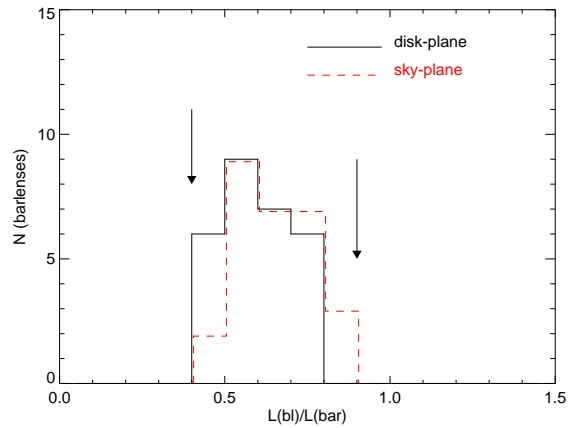
For simulations with no gas initially, e.g. gtr101, gtr102, gtr003 and gcs006, the barlens does not stand out sufficiently clearly for a two bar component fit to be necessary and decompositions with a single bar component can not be excluded. We therefore do not include these simulations in Tables 3 and 4 and defer further discussion to Sect. 7.5. There are also decomposition difficulties at the other extreme of the gas fraction, e.g. for gtr121, where the thin bar component is too weak and short to allow a reliable decomposition.

Table 4 has a layout similar to that of Table 2, but gives information on the barlens flux normalised either by the flux of the thin bar component (upper line for each simulation), or by the total flux (lower line). In some cases the thin bar component is very short and difficult to discern. In such cases the F_{bl}/F_{thin} takes very large values, but these are very unsafe because of the large uncertainties for F_{thin} . They should thus be used only with caution. This is certainly the case for the two first times for gcs004 and even for the three earlier times for gtr119. For such cases, and also more generally, the F_{bl}/F_{tot} values are much safer to use. These globally show an increase with time, which can be understood from the general growth of the bar during the secular evolution phase (Athanassoula 2013, for a review), which should be followed by an increase of its barlens component and is in good agreement with the known correlation between bar and peanut strength (Athanassoula 2008).

6.3.3 Decomposition tests

We have so far discussed simulation images only for face-on cases with the bar major axis along the x axis. Here we will present decomposition results for different viewing angles. For this we used simulation gtr111 at $t=6$ Gyr and viewed the snapshot after a rotation in the disc plane, to put the galaxy major axis at a different angles with respect to the bar major axis. We then inclined it by another angle. The results are given in Table 5. The first two columns give the viewing angles, the third one gives the axial ratio of the barlens component as obtained from the ellipse fits and the last two give the relative barlens fluxes. Also, as usual the shape parameter and the α and β parameters in the Ferrers function were left free for fitting.

As already discussed, this simulation galaxy has a near-circular barlens, with an axial ratio of 0.96, i.e. only slightly elongated along the bar major axis. If we keep the bar position angle to 0° and change the inclination angle to 30° (60°), we find that the axial ratio decreases to 0.77 (0.64). If the central component had

**Figure 5.** Number histogram of the minor-to-major axis ratios of barlenses in the NIRS0S Atlas. Again, the arrows mark the minimum and maximum of this parameter in our simulation models (in the plane of the disc).**Figure 6.** Number histogram of the sizes of barlenses for the galaxies in the NIRS0S Atlas, normalised to bar length. The black full line shows the measurements in the disc plain, and the (red online) dashed line the same galaxies in the sky-plane. The arrows indicate the minimum and maximum of the same parameter in our simulation models (in the disc plane). The sizes of structures are measured in a similar manner for the simulation models and for the observed galaxies.

been a near-spherical classical bulge, then no decrease would have been witnessed. On the contrary, if the central component was an axisymmetric thin disc we would find an axial ratio of 0.87 (0.5), or 0.84 (0.48) if it was slightly elongated along the bar major axis. Thus the geometry of this central part is certainly not spherical, but it has to be somewhat thicker than a thin disc. In Sect. 7.2 we will see that this is indeed the case.

7 DISCUSSION

7.1 Range of values for the barlens relative lengths and axial ratios

Let us now compare the range of values for the axial ratios of the barlens components in observations and in simulations. The former can be found for all galaxies with a barlens component in Table 5 of Laurikainen *et al.* (2011) and their histogram is plotted

here in Fig. 5, both in the sky-plane and in the galactic disc plane. The ellipticities for the simulations have been obtained from the ellipse fits described in Sect. 5. These simulations, however, were made in order to understand the effect of gas and the dark matter halo on the bar formation and evolution and do not necessarily cover the parameter space in the same way as the barred galaxies in NIRSOS. Furthermore the deprojection of observed galaxies, particularly barred, always entails some uncertainty. It is thus more meaningful to compare the range of allowed values than the whole histogram. We find that the ellipticities obtained for barlenses in our simulation models (marked with arrows) fit well the range defined by the observations. Furthermore, barlens ellipticities of the gtr models with initial gas fractions of 0.5, 0.75 or 1.00, are within the range of 0.7–1.0, where the peak in the observed ellipticities is found.

The distribution of barlens sizes, normalised to the bar length, as obtained from the NIRSOS sample, are shown in Fig. 6, again given separately for the disc and the sky planes. Again, the comparison of the ranges of the values obtained from simulation to the observed ones is most satisfactory.

7.2 The side-on view

Simulations have an important advantage over observations in that they allow the viewing of an object from any desired viewing angle. We will use this here in order to study the 3D structure of the barlens component. In Fig. 7 we show two snapshots viewed from three different angles. The snapshots correspond to the disc component of simulations gtr116 and gcs001, both at $t=6$ Gyr. In the lower panels they are viewed face-on and in the upper ones edge-on. The middle panels correspond to an intermediate viewing angle of 45° . In all cases the bar is oriented along the x axis, to facilitate comparisons. These two snapshots were chosen because they are good examples of specific morphological features which we wish to discuss here.

The face-on and intermediate views in Fig. 7 show that the edge of the barlens component at and around the direction of the bar minor axis is sharply defined, as witnessed by the crowding of the isodensities in that region, arguing for a corresponding sharp density decrease. Thus the name ‘lens’ is well deserved, since lenses should by definition have sharp edges (Kormendy 1979). This is in good agreement with the strong decrease of the surface density in the barlens region seen on the minor axis profiles in Figs. 2.

A further interesting point to note is the difference that the inclination makes to the shapes of both the thin bar component and the barlens. This can be clearly seen by comparing the shape of the isodensities in the face-on and the intermediate view. The thickness of the bar along the direction of its minor axis on the face-on view has a maximum at $x=0$ then decreases with increasing distance from the centre and reaches a minimum before increasing again. For example for gcs001 at $t=6$ Gyr (right panel of Fig. 7), the minimum thickness of the projected surface density iso-contours occurs somewhere around 4 kpc from the centre (measured along the bar major axis). Then the bar outline starts becoming thicker again. Thus one can describe this in short as a bulging inner part, thinning down as the distance from the centre increases, only to thicken again in the form of ansae. This is not visible in the intermediate view (inclination angle of 45°), where the whole bar shape is quite rectangular-like, presumably due to the projected contribution of the B/P bulge which extends more than a kpc above the equatorial plane. Similar results can be seen in the left panel for gtr116 at $t=6$ Gyr.

The solid vertical line extending through all three panels shows the extent of the barlens, as measured from the ellipse fits (Sect. 5). There is also a vertical dotted line, which shows the horizontal extent of the B/P bulge as estimated from the edge-on view. From this it is clear that the end of the barlens coincides, to within the estimation accuracy, with the end of the B/P bulge. In fact in some cases, as e.g. gcs001 at $t=6$ Gyr (right panel of Fig. 7), the two estimates coincide to within the thickness of the lines in the plot, so that no dotted line can be seen. To get a quantitative estimate, we repeated this exercise for a number of snapshots (simulations and times) and always found the same qualitative result. We found that both the median and the mean of the ratios of the extent of the barlens to that of the B/P bulge are equal to 0.95 with a variance of the distribution equal to 0.04, which is well compatible with the measurement errors. *This strongly argues that the barlens and the boxy/peanut bulge are one and the same component, and not two separate components, or two separate parts of the bar.*

We thus confirm that, as argued by Athanassoula (2005), bars are composed of two parts, an outer one being both vertically and horizontally thin, so that it can be called the thin bar component, and an inner one which is vertically thick and also fatter in the equatorial plane. This can be called the thick part of the bar, or the B/P/X bulge, or the barlens; both names describing the same part of the bar. Our finding here is in good agreement with previous works summarised in Sect. 2, but here we have demonstrated that the B/P/X component and the barlens component are in fact one and the same.

Our plots also allow us to obtain a rule of thumb that can give us information on the extent of the B/P/X/barlens component even when the galaxy is viewed near-face-on. Indeed, as already mentioned, the shape of the isophotes in the barlens region is very different from in the thin bar part. In the clearest of cases this makes the isophotes change curvature, from orienting their concave part towards the bar major axis to being rather flat, or orienting their convex part towards the bar major axis. The point or region where this change of curvature occurs gives a good estimate of the length of the barlens component. This rule of thumb works well near the face-on geometry, but it needs to be extended to be applicable to angles up to say 45° . Fig. 7 shows that for such orientations the end of the barlens is often better defined by the position at which the extent of the bar perpendicular to its major axis shows a clear change (decrease). It is also more reliable to use a number of isophotes, since some of them show this change in the in-plane thickness much clearer than others. For yet higher inclinations (i.e. nearer to edge-on) the vertical extent of the barlens makes it anyway easier to find its extent (Athanassoula & Beaton 2006; Erwin & Debattista 2013).

We checked our rule of thumb, by applying it to a number of snapshots seen from different viewing angles, and found that it fares very well for most reasonable morphologies, particularly after one’s eye has gained some expertise in detecting the correct features. There may, nevertheless, be some bar morphologies to which it can not be applied, such as fat bars with near-elliptical isodensities. Our rule of thumb is of course rather crude, but certainly safer than using a constant value for the ratio of the bar and barlens extents, as has been previously proposed, because as we saw in Sect. 7.1 the ratio of these two extents covers a wide range of values both in the observations and in the simulations.

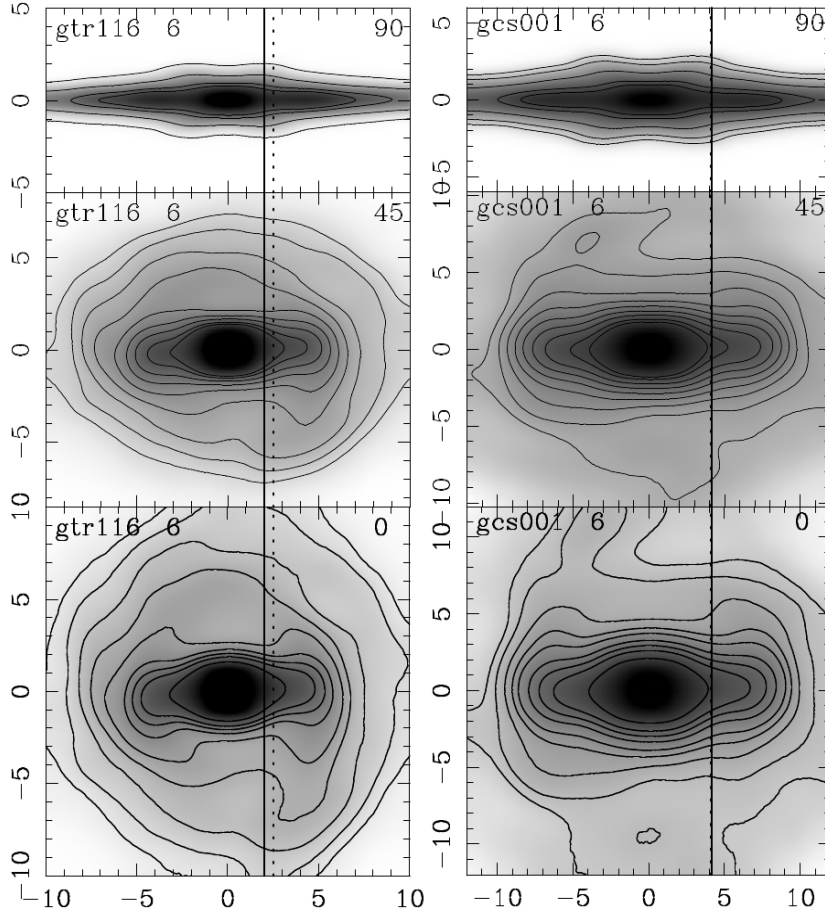


Figure 7. Grey-scale plots of three views of simulation gtr116 (left column) and gcs001 (right column), both at $t=6$ Gyr. In the lowest panels the simulations are viewed face-on, in the top one side-on and in the middle one at 45° . The grey scale levels are logarithmically spaced and the isodensities are at levels chosen to show best given morphological features discussed in the text. The vertical solid lines show the extent of the bar/ens component in all three views, as measured by the ellipse fits (Sect. 5). The vertical dashed lines show the extent of the B/P/X bulge. In the upper left corner of each panel we give the simulation name and snapshot time and in the upper right one the viewing inclination angle.

7.3 Can some barlenses be mistaken for classical bulges?

In Fig. 8 we view a further comparison between simulations and observations. The left panel shows an image of the barred galaxy NGC 936, obtained by combining the g, r and i images from the SDSS. The right panel displays gtr116 at time $t = 6$ Gyr, viewed from angles such that it mimics best NGC 936. The barlens and the thin bar component are very clearly seen in both cases. This simulation was not specifically run so as to model NGC 936, yet the bar regions in the observations and in the simulations have a very similar morphology. The most important thing to note, however, is that this simple visual inspection of the central region of both NGC 936 and the simulation could lead to the conclusion that both have a classical bulge, while at least for the simulation we are sure, by construction, that it has no classical bulge. It is thus clear that a barlens component can be mistaken for a classical bulge, if morphology is the only available information.

Could photometry reveal whether the inner component is a barlens or a classical bulge? Fig. 3 shows that, both in observations and in simulations, barlenses can produce a very sharp central peak in the radial luminosity profile which is reminiscent of that of a classical bulge. Thus the existence of such a peak can not allow us to distinguish between a classical bulge and a barlens component.

A possible way of distinguishing between these two alternatives could be colours, or population synthesis. Indeed, B/P/X bulges are formed from the vertical instabilities of the bar, i.e. such bulges are constituted of disc stars. In contrast, the most standard formation mechanism of classical bulges is from mergers occurring early on in the galaxy formation process, before the disc. Thus if the inner component is older and redder than the disc, then it should clearly be a classical bulge and not a barlens. This colour difference, however, is not a necessary condition, since classical bulges can also form from later occurring minor mergers or have later gas accretion (e.g. Aguerri, Balcells & Peletier 2001; Coelho & Gadotti 2011), in which cases they could be younger and bluer than the disc, or they could include a younger sub-population. Thus in some cases it will be possible to distinguish classical bulges from barlenses by their colours or with the help of population synthesis, but in others not.

Kinematic observations could help out here, and indeed Kormendy (1983, 1984) finds a large V_{max}/σ value for several barred galaxies, including NGC 936. This was confirmed further in a study by Kent & Glaudel (1989). The latter authors produced a bulge/bar/disc decomposition, with each of the components contributing a similar amount to the total luminosity, and claimed an acceptable fit of their model to the kinemat-

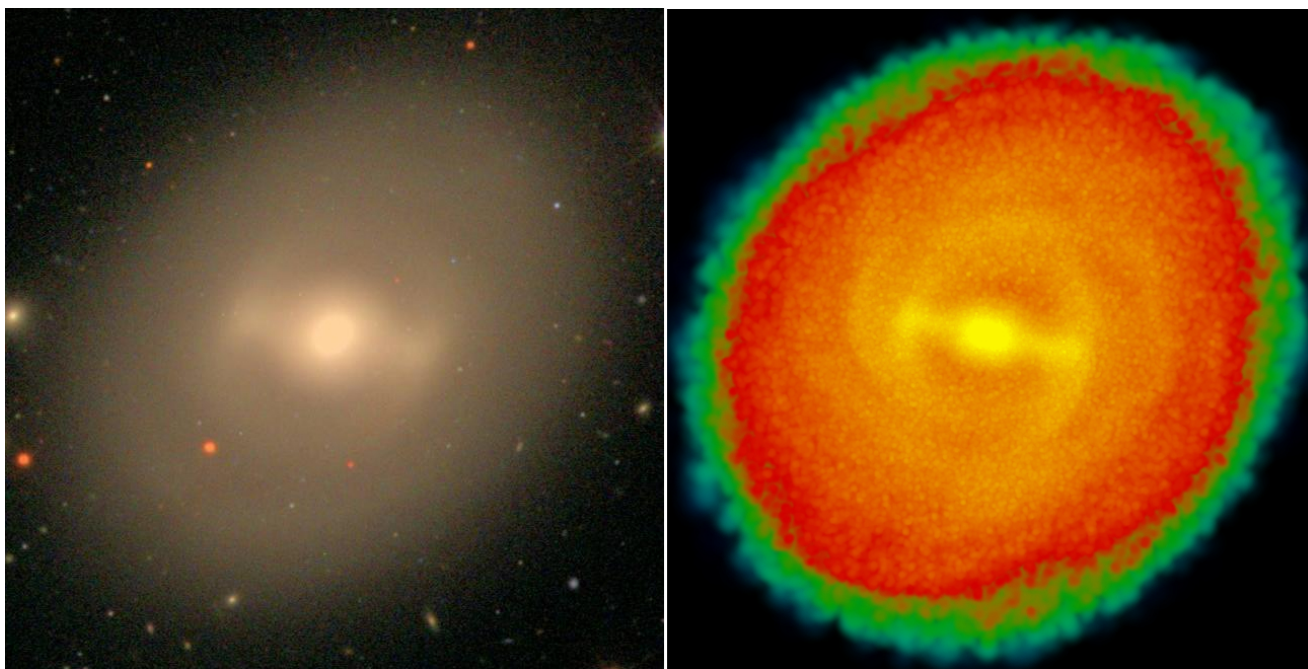


Figure 8. Comparison of a simulation snapshot (right panel) with an SDSS image of NGC 936 (Hogg, Blanton and the SDSS collaboration, as in the Near Extragalactic Database - NED). Note the resemblance between the two morphologies in the bar region. The simulation, however, has, by construction, no classical bulge component, the inner component being a barlens when viewed face-on and a B/P/X bulge when seen edge-on. We discuss the implication of this comparison in Sect. 7.3.

ics. However, their “bulge” component is triaxial, which probably indicates the influence of the bar. NGC 936 is also in the ATLAS3D sample and, indeed, the ATLAS3D collaboration found that it was not possible to model the observed kinematics by something intrinsically spheroidal and that some disc-like kinematics was necessary (Cappellari 2013, private communication, see www.eso.org/sci/meetings/2013/MORPH/Videos/Day-4/morph2013Athanasoula.mp4; see also Cappellari *et al.* 2011 and Cappellari *et al.* 2013). Thus detailed kinematical studies can distinguish between barlenses and classical bulges. Unfortunately though such detailed kinematics are available only for few galaxies. For the galaxies which are seen near to face-on and for which kinematics are not available, barlenses could still be mistaken for classical bulges.

Our results thus show that a fraction of the central components that are believed to be classical bulges will in fact be barlenses, or at least a part of their mass could be attributed to a barlens. This can have severe repercussions for studies of individual galaxies. For example, when using the surface density to calculate potentials and forces within a barred galaxy in view of studying its orbital structure or the gas flow in it, the difference between the vertical distribution of mass in barlenses and in classical bulges can make non-negligible differences in the results as well as the Q_b measure of the bar strength. Furthermore, it can bias statistical studies involving galaxy classifications, since it might erroneously move galaxies towards earlier types. Finally, this can introduce errors in studies of the relative luminosities of classical bulges, since there is no reason for the luminosity distribution of barlenses to be the same as that of classical bulges.

It is difficult to give a precise estimate of how often barlenses are, by mistake, classified as classical bulges. Laurikainen *et al.* (2013) showed that about 62 ± 9 (38 ± 9) per cent of early type SB (SAB) galaxies have a barlens component, while our Fig. 5 shows

that about 70 per cent of the barlenses have an axial ratio above 0.7. We thus reach a very rough estimate of 45 (30) per cent for the fraction of early type SB (SAB) galaxies which have a barlens that can be mistaken for a classical bulge. This is a very large fraction, but should be considered as an upper limit, because not all near-circular barlenses will be mistaken for classical bulges. Nevertheless, the bias could be very substantial if one made statistics of, for example, a specific sample of galaxies whose properties are such as to favour rounder barlenses.

This possible confusion between classical bulges and barlenses is important to keep in mind when using the results of photometric decomposition models. Here and in the accompanying observational paper (Laurikainen *et al.* 2014) we show that the barlens can constitute a large fraction in mass of the bar. This is clear for real galaxies from the middle panel of figure 5 of Laurikainen *et al.* (2014), and for simulated galaxies from our Table 3 and Sect. 7.4, the observational and simulation results being again in good agreement. Thus, when seeking certain types of information, e.g. the classical-bulge-to-total ratio, it is necessary to include the barlens as a separate component, as we did here and in Laurikainen *et al.* (2014). Otherwise the classical bulge component obtained from the decompositions could be strongly overestimated, because it will contain also the barlens (or a large fraction of it), i.e. a component grown out of the disc. In some cases disc/bar/bulge decompositions may even give evidence for the existence of a classical bulge, when in reality none is present.

From the above discussion it is clear that in a number of cases a classical bulge can be thought to exist when none is present, or its mass can be erroneously and substantially overestimated. Although a more quantitative study remains to be made, it is clear that the result of such misclassifications is a bias and not an error, so that the correct fraction of disc galaxies with no classical bulge will be larger than currently estimated, and the contribution of classical

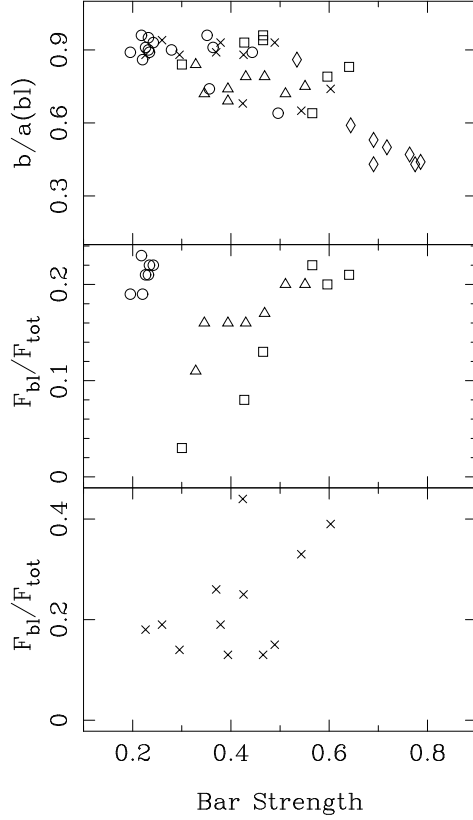


Figure 9. Trends between the bar strength and the barlens properties, more specifically the barlens axial ratio as obtained from the ellipse fits (upper panel), and its flux normalised by the total flux of the model as obtained by the decompositions (middle and lower panels). The upper panel includes all the runs from Tables 1 and 2. gcs simulations are plotted with an open circle, gtr101, gtr111 and 119 with open diamonds, squares and triangles, respectively and the remaining gtr runs with an X symbol. The middle panel includes all measurements from Table 4 and the symbols are as above. Finally, the lower panel includes all simulations from Table 3, all plotted with an X symbol.

bulges to the total mass budget less. It is important to note that this will render more acute the problems of Λ CDM concerning the formation of disc galaxies with no classical bulge, and it is unclear whether this can be resolved with yet stronger feedback.

7.4 Trends

In the upper panel of Fig. 9 we plot the axial ratio of the barlens component, as calculated from the ellipse fits described in Sect. 5 (Tables 1 and 2), as a function of the bar strength as calculated in AMR13, i.e. from the maximum of the relative $m=2$ Fourier component. The only trend visible is for the time evolution of simulation gtr101 (which has a very strong bar). The remaining evolution sequences as well as the results from all simulation snapshots at $t = 6$ Gyr show no clear trend. It is thus possible that for very strong

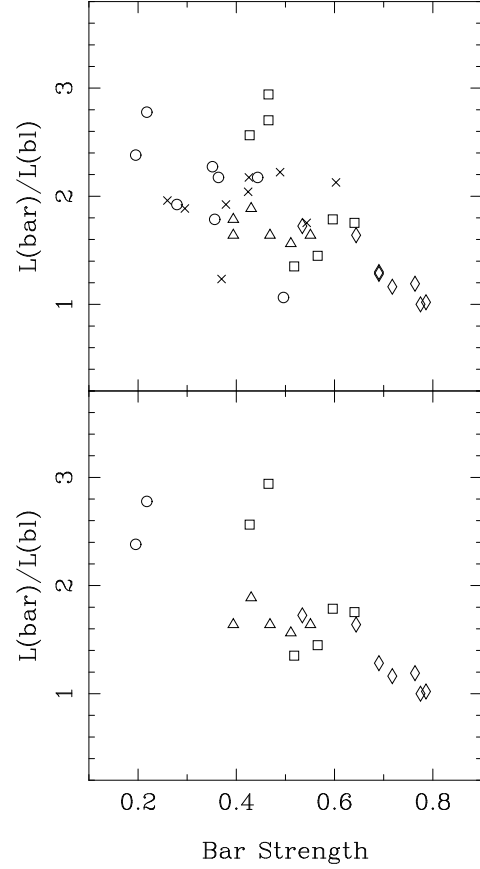


Figure 10. Trends between the bar strength and the ratio of the bar extent to the barlens extent. The upper panel includes all the runs from Tables 1 and 2 and the lower one only the data from Table 2, i.e. data from the evolution. Symbols are as in Fig. 9.

bars there is a trend, with barlenses being more elongated when the bar is stronger. It is also possible that all cases with a bar strength below a certain limit (0.3 in our models) have near-circular barlens components. In general, however, no clear trend has been found between barlens axial ratio and bar strength.

The middle and lower panels show the barlens flux normalised by the total flux as a function of bar strength. Simulation gcs004 (open circles) shows no evolution of the bar strength, due to its high initial gas content, coupled to its strong central cusp (AMR13 and Athanassoula 2013). Simulations gtr111 and gtr119 show a clear evolution of their bar strength as well as of their relative barlens flux. These two evolutions are stronger for the galaxy with less gas, as expected from the results in AMR13. Moreover, these evolutions are such that there is a clear trend between these two quantities, so that cases with stronger bars have also higher relative barlens fluxes. This trend can also be seen from the lower panel which includes all the simulations at $t=6$ Gyr. Again there is no strong correlation, but there is a trend.

Fig. 10 shows a further trend with the bar strength, namely for the ratio of the thin bar length to the peanut length, as given

in Tables 1 and 2. We find that the strongest bars have barlenses which extend to larger radii, as normalised by the bar length, i.e. they cover a bigger part of the bar major axis. This is particularly clear for the time evolutions (lower panel), but there is still a trend when we include all our data (upper panel). Similar trends are also found when we use in the abscissa the bar length instead of the bar strength, but since the quality of the trend is roughly similar we do not show it here.

Should we expect our predicted trends to be verified by observed galaxies? This is well possible, but far from sure. It should not be forgotten that observations may contain a much more diverse set of galaxy parameters than our models, with different masses, different disc velocity dispersions, cases with and without classical bulges, or a wider variety of halo mass distributions, etc, which could ‘dilute’ the trends. The answer to the above question – i.e. whether real galaxies verify our predictions – was given in the accompanying paper (Laurikainen *et al.* 2014) using a selected subsample of 10 to 15 galaxies from the NIRS0S and S⁴G samples. It is gratifying to note that their observational results are in good agreement with our predictions.

7.5 Orbital structure and barlenses

The first step for understanding the dynamics of any substructure is to study the orbits that constitute it. Of course no study of orbits in barlenses has so far been made, but if these structures are the face-on view of the B/P/X bulges, as argued in Sect. 7.2, the orbital structure of the latter (as discussed e.g. by Pfenniger 1984; Patsis *et al.* 2002, or Skokos, Patsis & Athanassoula 2002a) should be sufficient. The most likely building blocks for our case and the most widely discussed in the literature, will then be 3D families of periodic orbits of the x_1 tree which bifurcate from the vertical resonances of the 2D x_1 family and have stable parts of a sufficiently large extent. The families that bifurcate at the lowest energies – such as x_1v_1 , x_1v_3 , x_1v_4 , or x_1v_5 at the 2:1, 3:1 or 4:1 resonances – are the most likely candidates, since the outline of orbits from higher bifurcating families are less vertically extended and more elongated in the direction of the equatorial plane and thus less appropriate building blocks. An alternative would be the $z3.1s$ family, whose orbits have a morphology which similar to that of the x_1v_4 family but is not related to the x_1 tree. This, however, would be suitable only in specific models while B/P/X bulges are generally found in barred galaxies, so that this is not a likely alternative and we will not consider it further here.

Thus a wealth of information on the orbits constituting the barlens can already be found in the literature. Nevertheless, some care has to be taken when using these results. Indeed, as already discussed in previous sections, real bars have a very complex morphology and geometry, such that their potential has not been yet adequately modelled by an analytic function. The most realistic of the existing analytic models, the Ferrers models (Ferrers 1877), have an ellipsoidal shape, which is not a good description of the real bar shape, and, viewed edge-on, do not have a B/P/X. Yet, for lack of any better potential/density model, Ferrers models have been used in most orbital structure studies of the barlens/bar/bulge region (e.g. Athanassoula *et al.* 1983; Papayannopoulos & Petrou 1983; Pfenniger 1984; Athanassoula 1992; Skokos, Patsis & Athanassoula 2002a; Patsis 2005). Most probably the main qualitative results of these studies can be applied to real galaxies, but their quantitative results may be considerably off. It would therefore be highly desirable to make orbital structure studies in more realistic potentials,

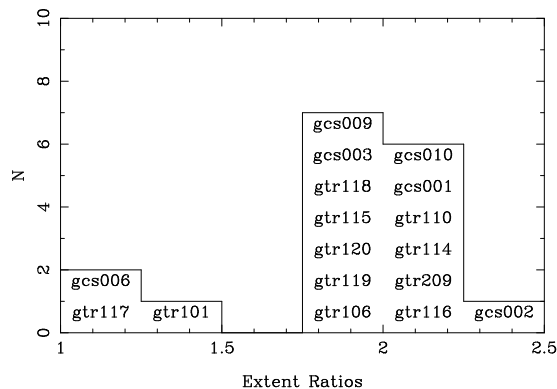


Figure 11. Histogram of the ratio of the extent of the thin part of the bar to the barlens extent. Within the histogram we mark the simulation names.

taking into account the 3D shape of the B/P/X/barlens component as well as the rectangularity of the thin bar component.

As mentioned above, orbits from families bifurcating from the x_1 at low energies (Jacobi constants) have an outline which is less elongated in the direction of the equatorial plane compared to that of the thin bar. Thus, by comparing the horizontal extent of the barlens to that of the thin bar component, it should in principle be possible to deduce which vertical resonance is the main contributor to the barlens and where it is located. In Table 1 we gave values for the ratio of the barlens extent to that of the thin bar component for the $t=6$ Gyr snapshots of all simulations treated here and in Fig. 11 we give a histogram of their inverse values. These are to be compared with the corresponding numbers in Tables 1 to 6 of Patsis *et al.* (2002). Fig. 11 shows that only 3 out of 17 models have $L(\text{bar})/L(\text{bl}) < 1.5$ and this is in agreement with the corresponding histogram for the NIRS0S galaxies which relatively few galaxies with $L(\text{bl})/L(\text{bar}) > 0.7$. Of course one can not do more detailed comparisons for two reasons. One is because the distribution of the simulations we are analysing in the parameter space is not necessarily the same as that of the galaxies in the same space. The second is that the orbital structure work was performed in potentials with Ferrers ellipsoids and, as we already discussed, this may bring considerable quantitative differences. Nevertheless, determining which of the vertical families is responsible for the barlens may still be within reach. Our histograms show that vertical families bifurcating from the x_2 family are rather unlikely. The most likely family is the x_1v_1 and the second best ones are the x_1v_3 , x_1v_4 and x_1v_5 .

The barlens and the thin bar component can be considered as two components, or as two sub-components of the bar. Either way, they are not independent, because their properties are tightly linked. Thus at all times they have the same position angle, which implies that they rotate with the same pattern speed and that their resonances, as defined by the simple linear definition, overlap. Moreover, it is the vertical instabilities of the thin bar component orbits that generate the families of periodic orbits that are the backbone of the thick bar component, i.e. the barlens component. Even though these two components are tightly linked, it is necessary for the galaxy decompositions to include an additional bar component, because of the very complex geometrical shape of the bar, which, can not be well approximated by a single bar component but in

most cases, can be reasonably approximated by adding a lens-like component to the thin bar component.

Skokos, Patsis & Athanassoula (2002a) noted that the (x, y) projections of the 3D families of the x_1 -tree, i.e. the $x_1 v_n, n = 1, 2, 3, \dots$ families, retain a morphological similarity with the parent x_1 family at the same energy. In particular, in regions relatively near the bifurcating points their face-on shapes are actually very close to the x_1 shape. That could at first sight have been considered to disagree with the fact that the face-on outlines of the barlens are very different from that of the thin bar components, and thus argue against the barlens picture that we propose here. It must, however, be kept in mind that the orbital structure study of Skokos, Patsis & Athanassoula (2002a), like those of all other such studies, is carried out using Ferrers potentials and do not include the potential of a separate barlens components. This is a further argument underlining the necessity of orbital structure studies using yet more realistic potentials.

8 SUMMARY AND CONCLUSIONS

In this paper we used snapshots of barred disc galaxy simulations to make images, which we then analysed using the same procedures and software as for the analysis of real galaxy images in previous studies. We found that our simulations can produce bar components whose properties are comparable to those of the observed barlenses. By making a number of comparisons between simulations and observations, including morphology, radial projected density profiles, shapes obtained from ellipse fits and decomposition results, we find excellent agreements and thus reach the conclusion that our simulations are sufficiently realistic to describe accurately components such as barlenses.

Viewing our simulations edge-on we were able to explore the nature of the barlens component and to find that the barlens and the B/P/X bulge are one and the same component, but viewed from a different angle. We found this to be true not only for elongated barlenses, but also for the case of circular-like ones.

This result concerning the nature of the barlens component implies that the distribution of the z -component of the velocity of stars in the barlens should be that of a thick object while that of the stars in the thin component should be that of a vertically thin one. It should be possible to test this prediction by measuring the vertical velocity component along the bar major axis of appropriately chosen face-on barred galaxies. One should then find a much higher velocity dispersion σ_z and a different structure of the higher velocity moments in the thick barlens component compared to the thin part of the bar. It is not, however, necessary to expect that there should be a sharp transition between the two regions. Indeed, in Sect. 4 we found that there is no such sharp transition in the radial luminosity profile and attributed this to the fact that the thin bar component continues inwards into the barlens region so that in the region surrounding the bar major axis and within the barlens component there will be contributions from both components.

Our result has a further implication, namely that it can set a rough lower limit of the bar age and a very clear one on the phase of evolution the bar is in. Indeed, the fact that the barlens and the boxy/peanut bulge are one and the same component implies that for the barlens to exist, the B/P/X must have already formed and the bar must be in the secular evolution phase, i.e. between one and a few Gyr must have elapsed from the moment it started forming.

The statistical study of Laurikainen *et al.* (2013) found barlenses only in a fraction of barred galaxies. Yet it is usually implic-

itly assumed that all barred galaxies, had they been observed edge-on would show a B/P/X bulge. The disagreement between these two statements is only apparent, as can be understood in two different ways. Firstly, simulations show that B/P/X bulges form *after* the bar. In the few cases where this has been measured, the time lapse between bar and peanut formation was found to be of the order of a couple to a few Gyr (e.g. Combes *et al.* 1990; Athanassoula 2008). Any galaxy observed during that time would have a bar, but no peanut. Further work, however, is necessary to find what fraction of observed bars could be sufficiently young not to have yet formed a B/P/X bulge, how this depends on the main galaxy parameters (halo properties, gas fraction, existence of a classical bulge etc.) and whether these results agree with the statistical results of Laurikainen *et al.* (2013). Secondly, it could be that there is a barlens in all strongly barred galaxies, but that in some cases this is not easily discernible by eye, e.g. because its extent along the bar minor axis is not sufficiently larger than that of the corresponding thin bar component. Again here more work is necessary, now using orbital structure studies in order to understand what determines the face-on shape of the barlens component.

We also found that the morphological and photometrical properties of the barlens component are such that in some cases it can be mistaken for a classical bulge. Thus the number of galaxies with no classical bulge can be much higher than what has been so far assumed and also that in many galaxies the contribution of the classical bulge to the total mass budget is substantially overestimated. This will introduce errors in dynamical studies of some individual galaxies and a bias in a number of statistical studies. We propose that colours and particularly kinematics can be used to discern between classical bulges and barlenses.

Our work made also clear how necessary two further studies are. The first one is to revisit considerable part of orbital structure studies and gas flow calculations, using yet more realistic potentials, taking into account the complex 3D structure of bars and including the B/P/X/barlens component. The second one concerns decompositions of real barred galaxies. Indeed the description of a bar with a barlens by a single bar component will necessarily introduce errors which can in many cases be very substantial. This is made clear for simulations in this paper and for real galaxies in Laurikainen *et al.* (2014). It is thus necessary to repeat a number of the previous studies, using now a decomposition including two bar components, i.e. a barlens and a thin bar component, in order to be able to obtain more accurate bar parameters and thus be able to better track secular evolution.

Further support for our work is given in an accompanying observational paper (Laurikainen *et al.* 2014). This work used the S⁴G and the NIRS0S samples to examined in particular B/P/X components and barlenses. Laurikainen *et al.* considered the distribution of galaxies as a function of their inclination angle, separately for galaxies having B/P/X components and for galaxies having barlenses. Adding the two populations together they found a flat total distribution, consistent with our finding that in simulations the two are the same component, but seen from a different orientation. They also made decompositions including the barlens component for 30 galaxies and found that they have small or non-existent classical bulges, again in good agreement with our discussion in Sect. 7.3. There is thus very good agreement between the theoretical and observational works, which, together, provide crucial information on the nature of the barlens component.

ACKNOWLEDGEMENTS

It is a pleasure to thank Volker Springel for making available to us the version of GADGET used here. All authors acknowledge financial support to the DAGAL network from the People Programme (Marie Curie Actions) of the European Union's Seventh Framework Programme FP7/2007-2013/ under REA grant agreement number PITN-GA-2011-289313. EA and AB also acknowledge financial support from the CNES (Centre National d'Etudes Spatiales - France). EL and HS acknowledge support from the Academy of Finland. Part of the simulation work described here was performed using HPC resources from GENCI-TGCC/CINES (Grants 2013 - x2013047098 and 2014 - x2014047098). This research is based in part on observations made with the Spitzer Space Telescope, which is operated by the Jet Propulsion Laboratory, California Institute of Technology under a contract with NASA. Funding for the SDSS and SDSS-II has been provided by the Alfred P. Sloan Foundation, the Participating Institutions, the National Science Foundation, the U.S. Department of Energy, the National Aeronautics and Space Administration, the Japanese Monbukagakusho, the Max Planck Society, and the Higher Education Funding Council for England. The SDSS Web Site is <http://www.sdss.org/>. The SDSS is managed by the Astrophysical Research Consortium for the Participating Institutions. The Participating Institutions are the American Museum of Natural History, Astrophysical Institute Potsdam, University of Basel, University of Cambridge, Case Western Reserve University, University of Chicago, Drexel University, Fermilab, the Institute for Advanced Study, the Japan Participation Group, Johns Hopkins University, the Joint Institute for Nuclear Astrophysics, the Kavli Institute for Particle Astrophysics and Cosmology, the Korean Scientist Group, the Chinese Academy of Sciences (LAMOST), Los Alamos National Laboratory, the Max-Planck-Institute for Astronomy (MPIA), the Max-Planck-Institute for Astrophysics (MPA), New Mexico State University, Ohio State University, University of Pittsburgh, University of Portsmouth, Princeton University, the United States Naval Observatory, and the University of Washington.

REFERENCES

- Aguerri, J. A. L., Balcells, M., Peletier, R. F. 2001, *A&A*, 367, 428
- Athanassoula, E., 1992, *MNRAS*, 259, 328
- Athanassoula, E., 2005, *MNRAS*, 358, 1477
- Athanassoula, E., 2006, arXiv:astro-ph/0610113
- Athanassoula, E., 2008, in "Formation and Evolution of Galaxy Bulges", Proceedings of the International Astronomical Union, IAU Symposium, 245, 93
- Athanassoula, E., 2013, in "Secular Evolution of Galaxies", J. Falcón-Barroso and J. Knapen (eds.), Cambridge University Press, Cambridge, UK, 305.
- Athanassoula, E., Beaton, R. L. 2006, *MNRAS*, 370, 1499
- Athanassoula, E., Bienaymé, O., Martinet, L. & Pfenniger, D. 1983, *A&A*, 127, 349
- Athanassoula, E., Machado, R. E. G., & Rodionov, S. A. 2013, *MNRAS*, 429, 1949 (AMR13)
- Athanassoula, E., Misiriotis A., 2002, *MNRAS*, 330, 35
- Athanassoula, E., Morin, S., Wozniak, H., Puy, D., Pierce, M. J., Lombard, J., Bosma, A. 1990, *MNRAS*, 245, 130
- Beaton, R. L., Majewski, S. R., Guhathakurta, P., Skrutskie, M. F., Cutri, R. M., Good, J., Patterson, R. J., Athanassoula, E., Bureau, M. 2007, *ApJ*, 658, 91L
- Benjamin, R. J. et al., *ApJ*, 630, L149
- Bettoni, D., Galletta, G., 1994, *A&A*, 281, 1
- Binney, J. 1978, *MNRAS*, 183, 501
- Bureau, M., Aronica, G., Athanassoula, E., Dettmar, R.-J., Bosma, A., Freeman, K. C. 2006, *MNRAS*, 370, 753
- Buta, R. 2013a, Planets, Stars and Stellar Systems Vol. 6, Eds. Oswalt, Terry D.; Keel, William C., Springer Science+Business Media Dordrecht, 2013, p. 1
- Buta, R. 2013b, IAC Talks, Astronomy and Astrophysics Seminars from the Instituto de Astrofísica de Canarias, id.264
- Buta, R., Laurikainen E., Salo H., Block, D. L., Knapen J. H., 2006, *AJ*, 132, 1859
- Cabrera-Lavers, A., González-Fernández, C., Garzón, F., Hammersley, P.L., López-Corredoira, M. 2008, *A&A*, 491, 781
- Cabrera-Lavers, A., Hammersley, P. L., González-Fernández, C., López-Corredoira, M., Garzón, F., Mahoney, T. J. 2007, *A&A*, 465, 825
- Cappellari, M. *et al.* 2011, 416, 1680
- Cappellari, M. *et al.* 2013, 432, 1862
- Churchwell, E., Babler, B.L., Meade, M.R., Whitney, B.A., Benjamin, R., Indebetouw, R., Cyganowski, C., Robitaille, T.P., Povich, M., Watson, C., Bracker, S. 2009, *PASP*, 121, 213
- Coelho, P., Gadotti, D. A. 2011, *ApJ*, 743, 13
- Combes, F., Debbasch, F., Friedli, D., Pfenniger D., 1990, *A&A*, 233, 82
- Contopoulos, G., Papayannopoulos, T. 1980, *A&A*, 92, 33
- Elmegreen B. G., Elmegreen D. M., 1985, 1985, *ApJ*, 288, 438
- Erwin, P., Sparke, L. 2003, *ApJS*, 146, 299
- Erwin, P., Debattista, V. 2013, *MNRAS*, 431, 3060
- Ferrers N. M. 1877, *Q.J. Pure Appl. Math.*, 14, 1
- Gadotti, D. A., 2009, in 'Chaos in Astronomy', G. Contopoulos and P. Patsis (eds), Springer Berlin Heidelberg, 159
- Gadotti D. A., 2011, *MNRAS*, 415, 3308
- Hammersley, P. L., Garzón, F., Mahoney, T. J., López-Corredoira, M., M.A.P. Torres, M. A. P. 2000, *MNRAS*, 317, L45
- Hernquist L., 1993, *ApJS*, 86, 389
- Kent, S., Glauzel, J. 1989, *AJ*, 98, 1588
- Kormendy J. 1979, *ApJ*, 227, 714
- Kormendy J. 1983, *ApJ*, 275, 529
- Kormendy J. 1984, *ApJ*, 286, 183
- Laurikainen, E., Salo, H., Athanassoula, E., Bosma, A., Herrera Endoqui, M. 2014, *MNRAS*, *subm.*
- Laurikainen, E., Salo, H., Athanassoula, E., Bosma, A., Buta, R., Janz, J. 2013, *MNRAS*, 430, 3489
- Laurikainen, E., Salo, H., Buta, R., Knapen, J. 2007, *MNRAS*, 381, 401
- Laurikainen, E., Salo, H., Buta, R., Knapen, J. 2011, *MNRAS*, 418, 1452
- Laurikainen, E., Salo, H., Buta, R., Knapen, J., Comerón, S. 2010, *MNRAS*, 405, 1089
- López-Corredoira, M., Cabrera-Lavers, A., Mahoney, T.J., Hammersley, P.L., Garzón, F., González-Fernández, C. 2007, *AJ*, 133, 154
- Lütticke, R., Dettmar, R.-J., Pohlen, M., 2000, *A&A*, 362, 435
- Martínez-Valpuesta, I., Gerhard, O. 2011, *ApJL*, 734, L20
- Martínez-Valpuesta, I., Knapen, J., Buta, R. 2007, 134, 1863
- Navarro J.F., Frenk C.S., White S.D.M., 1996, *ApJ*, 462, 563
- Navarro J.F., Frenk C.S., White S.D.M., 1997, *ApJ*, 490, 493
- Papayannopoulos, T., Petrou, M. 1983, *A&A*, 119, 21
- Patsis, P. A., 2005, *MNRAS*, 358, 305

- Patsis, P. A., Skokos, Ch., Athanassoula, E. 2002, MNRAS, 337, 578
- Peng, C. V., Ho, L. C., Impey, C. D., Rix, H.-W. 2010, AJ, 139, 2097
- Pfenniger, D. 1984, A&A, 134, 373
- Quillen, A. C., Kuchinski, L. E., Frogel, J. A., DePoy, D. L., 1997, ApJ, 481, 179
- Rodionov S. A., Athanassoula E., 2011, A&A, 529, A98
- Rodionov S. A., Athanassoula E., Sotnikova N. Y., 2009, MNRAS, 392, 904
- Romero-Gómez, M., Athanassoula, E., Antoja, T., Figueras, F. 2011, MNRAS, 418, 1176
- Salo, H. et al 2014, in prep.
- Sandage, A. 1961, The Hubble Atlas of Galaxies (Washington: Carnegie Institution)
- Sheth, K. et al. 2010, PASP, 122, 1379
- Skokos, Ch., Patsis, P. A., Athanassoula, E. 2002a, MNRAS, 333, 847
- Skokos, Ch., Patsis, P. A., Athanassoula, E. 2002b, MNRAS, 333, 861
- Springel V., 2005, MNRAS, 364, 1105
- Springel V., Hernquist L., 2002, MNRAS, 333, 649
- Springel V., Hernquist L., 2003, MNRAS, 339, 289
- Springel V., Yoshida N., White S. D. M., 2001, NewA, 6, 79
- Wakamatsu, K. I., Hamabe, M. 1984, ApJS, 56, 283